Journal of Materials Chemistry A

ROYAL SOCIETY OF CHEMISTRY

PAPER

View Article Online
View Journal | View Issue

Cite this: J. Mater. Chem. A, 2023, 11, 149

In situ surface-trap passivation of $CuBi_2O_4$ photocathodes for unbiased solar water splitting†

Yingfei Hu, [ab] Jun Wang,[a] Huiting Huang, [ac] Jianyong Feng,*[ac] Wangxi Liu, [a] Hangmin Guan, [b] Lingyun Hao,[b] Zhaosheng Li *[ac] and Zhigang Zou[a]

Passivating surface traps plays a crucial role in mitigating the efficiency loss of solar water-splitting electrodes. However, the associated surface-trap passivation approaches require the introduction of an overlayer, complicating the fabrication process and increasing the capital cost of photoelectrodes. Herein, using $CuBi_2O_4$ as a prototype, an *in situ* surface-trap passivation strategy is developed, which yields a beneficial 90 mV anodic shift in hydrogen-evolution onset. Detailed mechanism investigations prove that the intentionally added Mg^{2+} ions in the precursor gradually segregate as MgO and enrich at the grain boundaries/surface of the $CuBi_2O_4$ multicrystalline, porous film during annealing, *via* which surface traps stemming from dangling bonds are spontaneously passivated; measurements of photovoltage generation characteristics and carrier lifetime validate the favorable roles of the MgO passivator in $CuBi_2O_4$ photocathodes. A bias-free water-splitting device is assembled using MgO-passivated $CuBi_2O_4$ and Mo-doped $BiVO_4$ as the photocathode and photoanode respectively in a tandem configuration, delivering a solar-to-hydrogen conversion efficiency of approximately 0.41%.

Received 9th September 2022
Accepted 30th November 2022

DOI: 10.1039/d2ta07117g

rsc.li/materials-a

Introduction

Photoelectrochemical (PEC) water splitting, which directly captures and converts renewable solar energy to green hydrogen, is a promising approach to mitigate the increasingly urgent energy crisis and severe environmental pollution stemmed from excessive consumption of fossil fuels.[1–7] To enable large-scale application of PEC water splitting, numerous efforts have been devoted to seeking and developing high-efficiency, earth abundant and stable semiconductor electrodes in the past few decades.[8–13] Metal oxides have attracted much attention due to their high crustal abundance and stability in ambient environments.[14–18] However, most of the metal oxides, such as TiO_2 (~3.0 eV),[19,20] WO_3 (~2.6 eV),[21,22] $BiVO_4$ (~2.4 eV),[23–28] and Fe_2O_3 (~2.1 eV),[29–34] show n-type semiconducting characteristics and thereby could serve as water-oxidation photoanodes. Comparatively, metal oxides with p-type conductivity and suitable for construction of water-reduction photocathodes are relatively limited, prohibiting the development of high-performance all oxide-based bias-free solar water splitting systems/devices.

Recently, a p-type metal oxide of $CuBi_2O_4$ was identified as a promising photocathode candidate, due to its favorable bandgap of about 1.8 eV, sufficiently positive flat band potential at about 1.2 V *vs.* the reversible hydrogen electrode (RHE) and air processibility.[35–37] In principle, $CuBi_2O_4$ could produce a water-reduction photocurrent of 19 mA cm^{-2} under AM 1.5 G 1-sun conditions, yet the reported performances of $CuBi_2O_4$ photocathodes are far from the theoretical value.[38,39] This phenomenon can be rationalized by the highly mismatched light penetration depths (about 280 nm for the 550 nm photon) and charge carrier diffusion lengths (10–50 nm) of $CuBi_2O_4$.[40–43] By shortening the migration lengths of minority carriers and increasing the volume ratio of the space-charge region to the electrode bulk, nanostructuring could be an available strategy to address the above issue for $CuBi_2O_4$ photocathodes.[44] However, unfavorable surface traps/states with energy levels in the band gap may develop for $CuBi_2O_4$ photocathodes upon nanostructuring, due to the increased densities of dangling bonds and defects, and contribute to Fermi level pinning thereby enhancing charge carrier recombination. Therefore, the beneficial effects of nanostructuring are generally cancelled out by the detrimental influences of surface traps/states, making nanostructured $CuBi_2O_4$ photocathodes less efficient for water reduction.

The above challenge faced by nanostructured $CuBi_2O_4$ photocathodes could be circumvented by depositing a thin passivation overlayer, as has been extensively investigated for

[a]Collaborative Innovation Center of Advanced Microstructures, National Laboratory of Solid State Microstructures, School of Physics, Nanjing University, 22 Hankou Road, Nanjing 210093, China. E-mail: fengjianyong@nju.edu.cn; zsli@nju.edu.cn

[b]School of Materials Engineering, Jinling Institute of Technology, 99 Hongjing Avenue, Nanjing 211169, China

[c]College of Engineering and Applied Sciences, Nanjing University, Nanjing 210093, China

† Electronic supplementary information (ESI) available. See DOI: https://doi.org/10.1039/d2ta07117g

α-Fe_2O_3 photoanodes.[45,46] Although this surface-trap passivation scheme is effective, it usually involves the use of complicated post-treatment processes such as atomic layer deposition, chemical bath deposition and physical vapor deposition. If the surface traps/states on nanostructured $CuBi_2O_4$ photocathodes could be *in situ* passivated/ameliorated during the electrode fabrication/formation procedure, it would be more intriguing and cost-effective. Herein, by introducing appropriate amounts of Mg^{2+} ions into the precursor solution, *in situ* developed MgO segregations during the annealing step locate at the surface/grain boundaries of $CuBi_2O_4$ and serve as effective surface-trap passivators. The resulting MgO-passivated $CuBi_2O_4$ photocathode shows improved H_2 evolution activity at more anodic potentials when compared to the pristine one, and meanwhile allows combination with the Mo-doped $BiVO_4$ photoanode to drive bias-free overall water splitting under light illumination.

Results and discussion

All $CuBi_2O_4$ photocathodes were synthesized *via* a metal–organic decomposition method; varied amounts of $Mg(NO_3)_2 \cdot 6H_2O$ were added into the precursor solution to form Mg-modified $CuBi_2O_4$ photocathodes. The fabrication process of Mg-modified $CuBi_2O_4$ photocathodes is schematically illustrated in Fig. 1a. Fig. 1b shows the PEC water reduction performances of $CuBi_2O_4$ and Mg-modified $CuBi_2O_4$ (with 1%, 3%, 5%, 7%, 10% of Mg) photocathodes in a KB_i electrolyte (pH 9.2) under AM 1.5 G simulated sunlight irradiation. As depicted by the *J–V* characteristics, when the introduced amounts of Mg are less than 3%, the water reduction activities of $CuBi_2O_4$ and Mg-modified $CuBi_2O_4$ photocathodes are essentially identical. Adding more Mg (5%, 7% and 10%) offers $CuBi_2O_4$ photocathodes with largely improved performances; among them, 5% and 7% of Mg-modified $CuBi_2O_4$ photocathodes deliver the highest onset potentials at about 1.15 V *vs.* RHE, and the latter electrode also shows the highest saturation photocurrent density of –0.2 mA cm^{-2} at 0.7 V *vs.* RHE. The photocurrent densities (at 0.7 and 1 V *vs.* RHE) and photocurrent onsets of $CuBi_2O_4$ and Mg-modified $CuBi_2O_4$ photocathodes are summarized in Fig. 1c and d. As 7% of introduced Mg affords the $CuBi_2O_4$ photocathode the highest photocurrent density along with a 90 mV positive shift in onset potential, it is denoted as Mg-$CuBi_2O_4$ hereafter and subjected to further characterization studies.

XRD patterns collected on $CuBi_2O_4$ and Mg-$CuBi_2O_4$ electrodes are shown in Fig. 2a and S1.† Besides signals from FTO substrates, all other diffraction peaks are readily assigned to tetragonal $CuBi_2O_4$ (JCPDS 42-0334). Interestingly, no observable shift of XRD peaks can be detected in Mg-$CuBi_2O_4$ electrodes compared to the pristine $CuBi_2O_4$ film, indicating that introduced Mg does not occupy Cu or Bi sites in the lattice of $CuBi_2O_4$. On the other hand, no MgO or its related phase/component can be resolved by XRD, possibly due to its low content in the Mg-$CuBi_2O_4$ composite electrode (Fig. S2†). Raman spectra of both $CuBi_2O_4$ and Mg-$CuBi_2O_4$ electrodes show sharp characteristic peaks of $CuBi_2O_4$ at 134, 261, 400, and 577 cm^{-1} (Fig. 2b), confirming the formation of well crystalline $CuBi_2O_4$ films; again, no Raman peaks belonging to MgO can be probed in the Mg-$CuBi_2O_4$ electrode. Therefore, it is hypothesized that the introduced low-content Mg in the Mg-$CuBi_2O_4$ electrode may exist in the form of MgO nanoparticles and distribute uniformly in the matrix of the $CuBi_2O_4$ film. Light harvesting efficiency measurements on $CuBi_2O_4$ and Mg-$CuBi_2O_4$ electrodes reveal their almost identical photon capturing abilities in the tested wavelength range, suggesting a minor contribution of MgO to the light absorption process of $CuBi_2O_4$ (Fig. 2c). In addition, both $CuBi_2O_4$ and Mg-$CuBi_2O_4$ electrodes display an absorption edge of *ca.* 682 nm, corresponding well to the bandgap of tetragonal $CuBi_2O_4$ (1.85 eV, Tauc plot in inset of Fig. 2c).

XPS characterization studies were carried out to investigate the compositions and chemical bond information of $CuBi_2O_4$ and Mg-$CuBi_2O_4$ electrodes. As shown in Fig. 2d, both electrodes display spin–orbit doublets at 953.7 and 933.8 eV along with two shake-up satellite peaks in the Cu 2p spectra,

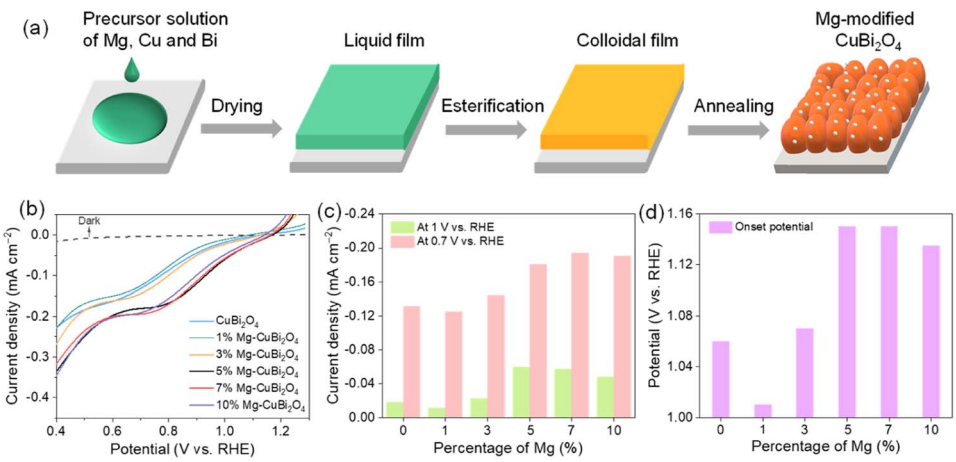

Fig. 1 (a) Schematic illustration of the synthetic process of Mg-modified $CuBi_2O_4$ photocathodes. (b) *J–V* curves of $CuBi_2O_4$ and Mg-modified $CuBi_2O_4$ photocathodes in KB_i (pH = 9.2); the corresponding (c) photocurrent densities at 0.7 and 1 V *vs.* RHE and (d) onset potentials.

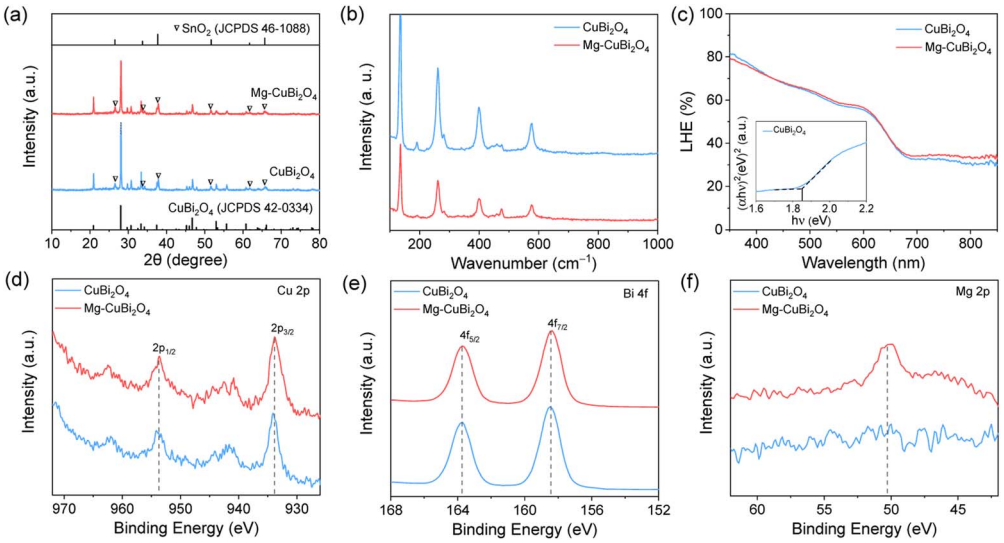

Fig. 2 (a) XRD patterns (triangles: peaks of FTO), (b) Raman spectra and (c) UV-vis absorption spectra (inset: Tauc plots, $(\alpha h\nu)^2$ as a function of $h\nu$) of $CuBi_2O_4$ and Mg-$CuBi_2O_4$ photocathodes. XPS spectra of (d) Cu 2p, (e) Bi 4f and (f) Mg 2p orbits in $CuBi_2O_4$ and Mg-$CuBi_2O_4$ samples.

suggesting an almost identical environment and oxidation state (+2) of Cu in them. In the Bi 4f region (Fig. 2e), both electrodes exhibit binding energies of 163.7 and 158.4 eV, which can be assigned to $4f_{5/2}$ and $4f_{7/2}$ of the Bi element with a valence state of +3. The O 1s spectra of the two electrodes can be deconvoluted into two peaks at 531.3 and 529.3 eV (Fig. S3†), which correspond to adsorbed hydroxyl species and lattice oxygen, respectively. As expected, a Mg signal is only detected on the Mg-$CuBi_2O_4$ electrode (Fig. 2f), the position of which (at ~50.6 eV) points to the presence of MgO. The above XPS analyses demonstrate that the chemical states of Cu, Bi and O in $CuBi_2O_4$ are not altered upon the introduction of Mg, and these Mg species form MgO instead of dopants in the $CuBi_2O_4$ film matrix.

As revealed by SEM observations, both $CuBi_2O_4$ and Mg-$CuBi_2O_4$ electrodes have porous structures, with particle sizes in the range of 100–300 nm (Fig. 3a and b and S4†). Such a film morphology is favorable for the collection of minority charge carriers. The firmly interconnected film particles along with high crystallinity, on the other hand, facilitate efficient transport of majority carriers in $CuBi_2O_4$ and Mg-$CuBi_2O_4$ electrodes.[47–49] In sharp contrast to the pristine $CuBi_2O_4$ electrode which exhibits a relatively smooth particle surface, a large quantity of white spots appear on the Mg-$CuBi_2O_4$ electrode. These nanoparticles could be *in situ* generated MgO segregations, the formation and distribution of which are confirmed by the energy dispersive X-ray spectroscopy (EDS) elemental mapping characterization studies.

To further investigate the characteristics of $CuBi_2O_4$ and Mg-$CuBi_2O_4$ electrodes, and probe the nature and distribution of the segregated nanoparticles in Mg-$CuBi_2O_4$, HR-TEM and EDS analyses were performed on $CuBi_2O_4$ and Mg-$CuBi_2O_4$ particles peeled from the corresponding electrodes. As depicted by Fig. S5†, sphere-like $CuBi_2O_4$ particles with a smooth surface are observed, and the measured lattice spacing of 0.190 nm agrees well with the (4 2 0) plane of tetragonal $CuBi_2O_4$. Bright diffraction spots are obtained in the selected area electron diffraction pattern, demonstrating the high crystallinity of $CuBi_2O_4$ particles, which is also consistent with XRD and

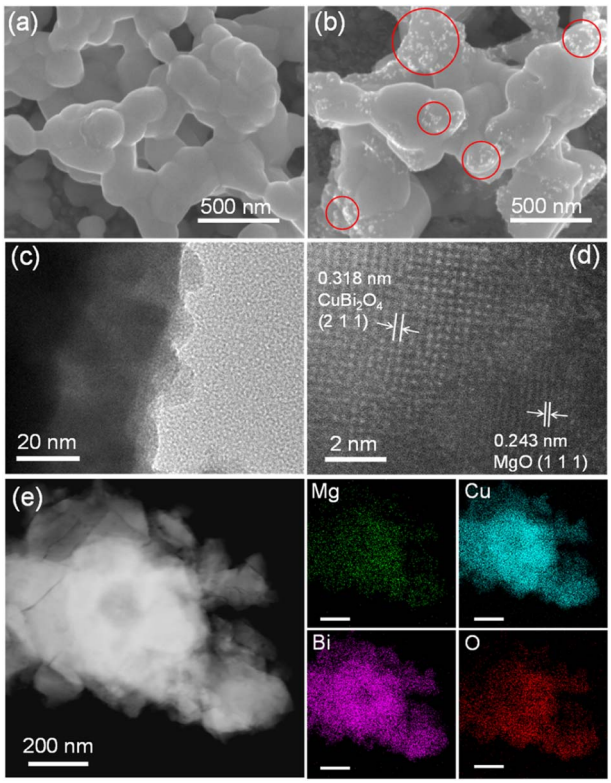

Fig. 3 SEM images of (a) $CuBi_2O_4$ and (b) Mg-$CuBi_2O_4$ films (several MgO particles are marked by red circles). (c) TEM (inset: SAED) and (d) HR-TEM images of Mg-$CuBi_2O_4$. (e) EDS elemental mappings of the Mg-$CuBi_2O_4$ sample (scale bar: 200 nm).

Raman characterization studies. In terms of Mg-$CuBi_2O_4$, particles with sizes of several to several tens of nm are observed to distribute randomly on the surface of Mg-$CuBi_2O_4$ particles (Fig. 3c), and the calculated interplanar spacing of 0.243 nm accords well with the (1 1 1) plane of MgO (Fig. 3d). Therefore, the introduced Mg in the Mg-$CuBi_2O_4$ electrode exists in the form of MgO nanoparticles, which distribute uniformly on the Mg-$CuBi_2O_4$ particle surface as demonstrated by EDS elemental mapping analyses (Fig. 3e and S6†).

To understand how the presence of segregated MgO nanoparticles affects the water reduction performance of the $CuBi_2O_4$ photocathode, charge separation efficiencies (η_{sep}) of $CuBi_2O_4$ and Mg-$CuBi_2O_4$ photocathodes were measured. As shown in Fig. 4a, the η_{sep} values of the Mg-$CuBi_2O_4$ photocathode are higher than those of the pristine $CuBi_2O_4$ photocathode at all applied potentials. Specially, η_{sep} of the Mg-$CuBi_2O_4$ photocathode increases from 0.5% at 1.1 V *vs.* RHE to 5.4% at 0.6 V *vs.* RHE, while those for the $CuBi_2O_4$ photocathode are 0.1% at 1.1 V *vs.* RHE to 3.2% at 0.6 V *vs.* RHE, respectively. The larger ΔOCP (difference of open-circuit potential in the dark and under light) of the Mg-$CuBi_2O_4$ photocathode (0.213 V) than that of the pristine $CuBi_2O_4$ photocathode (0.086 V) further confirms the enhanced charge separation and band bending of Mg-$CuBi_2O_4$ compared to $CuBi_2O_4$ (Fig. 4b). Furthermore, the measurement of ΔOCP also provides a means to extract charge carrier recombination lifetimes and thereby understand the quality of the electrode/electrolyte junction. Under open-circuit conditions, upon switching from the quasi-equilibrium of illumination to the dark equilibrium, the charge carrier recombination is largely dominated by the built-in electric field (band bending) of the space charge layer. The larger the band bending is, the faster the charge carrier recombination occurs at the transient of light-off. The charge carrier recombination lifetime is quantified using the following equation:

$$\tau = -\frac{k_B T}{e}\left(\frac{d\Delta OCP}{dt}\right)^{-1}$$

where τ is the charge carrier recombination lifetime, k_B is the Boltzmann constant, T is the temperature and e is the elementary charge.[50] As shown in Fig. 4c, the calculated carrier recombination lifetime for the pristine $CuBi_2O_4$ photocathode is *ca.* 100 ms at the transient of light-off under open-circuit conditions. Comparatively, under the same conditions the carrier recombination lifetime of the Mg-$CuBi_2O_4$ photocathode is *ca.* 26 ms. Therefore, the faster ΔOCP decay kinetics of the Mg-$CuBi_2O_4$ photocathode demonstrates the better quality of the electrode/electrolyte junction (or larger band bending) than that of the pristine $CuBi_2O_4$ photocathode. The substantially enhanced photovoltage generation of the Mg-$CuBi_2O_4$ electrode at above-bandgap excitation than that of the pristine $CuBi_2O_4$ electrode further supports this hypothesis (Fig. 4d).

Using Mott–Schottky analysis, the possible effects of Mg as an acceptor-type dopant have been excluded (Fig. S7†). It is therefore reasonable to propose that these segregated MgO

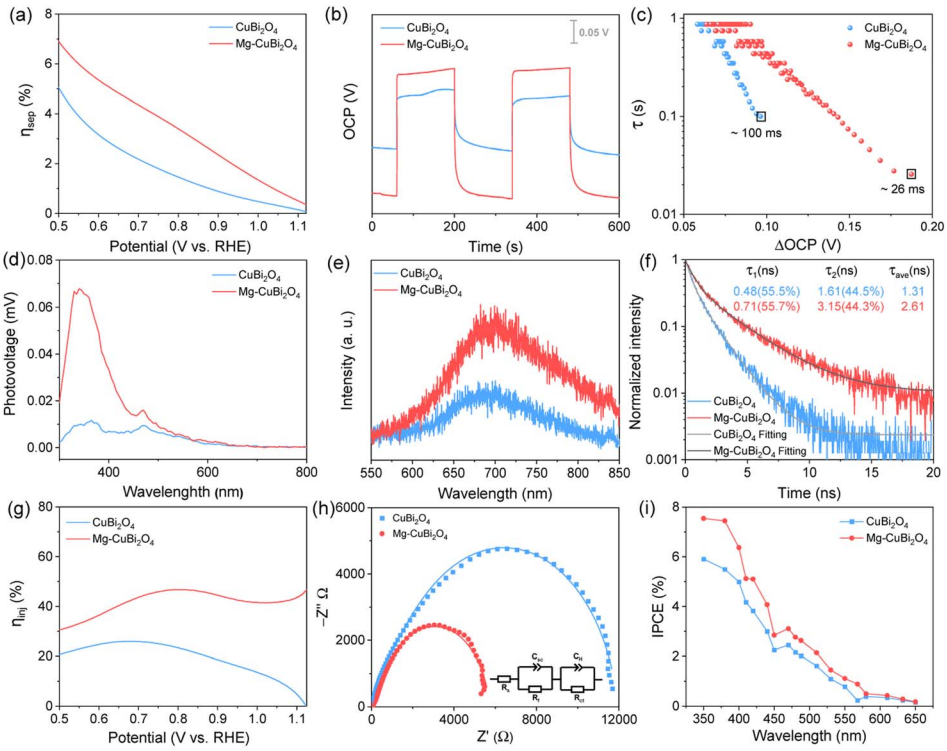

Fig. 4 (a) Charge separation efficiency (η_{sep}), (b) open-circuit potential (OCP) values, (c) carrier lifetime as a function of ΔOCP originated from OCP-decay curves when turning off light, (d) surface photovoltage curves, (e) steady-state PL spectra, (f) TRPL spectra, (g) surface charge injection efficiency (η_{inj}), (h) Nyquist plots (inset: the equivalent circuit for the samples), and (i) IPCE spectra of the $CuBi_2O_4$ and Mg-$CuBi_2O_4$ photocathodes.

nanoparticles may play a role in surface-trap passivation, *via* which Fermi level pinning is lessened and band bending (built-in electric field) in the Mg-$CuBi_2O_4$ photocathode is enhanced. Photoluminescence (PL) and time-resolved PL (TRPL) measurements were conducted to investigate the defects and trap states in $CuBi_2O_4$ and Mg-$CuBi_2O_4$ electrodes. Both $CuBi_2O_4$ and Mg-$CuBi_2O_4$ samples exhibit a PL emission peak at 692 nm, which agrees well with the bandgap of tetragonal $CuBi_2O_4$. Compared to pristine $CuBi_2O_4$, enhanced PL intensity is obtained on the Mg-$CuBi_2O_4$ sample (Fig. 4e). Meanwhile, the carrier lifetime of Mg-$CuBi_2O_4$ (2.61 ns) extracted from its exponentially decayed TRPL signal is about twice that of pristine $CuBi_2O_4$ (1.31 ns), as shown in Fig. 4f. The greatly enhanced PL intensity and prolonged PL lifetime of Mg-$CuBi_2O_4$ over $CuBi_2O_4$ suggest that the presence of segregated MgO nanoparticles indeed leads to a reduced density of trap states and a suppressed carrier recombination rate in the Mg-$CuBi_2O_4$ photocathode.

The surface water reduction behaviors of $CuBi_2O_4$ and Mg-$CuBi_2O_4$ photocathodes were evaluated by probing their charge injection efficiency (η_{inj}) curves (Fig. 4g). Substantially increased η_{inj} values are observed on the Mg-$CuBi_2O_4$ photocathode compared with the pristine $CuBi_2O_4$ photocathode, especially at more positive potentials. Specifically, at an applied potential of 0.6 V *vs.* RHE, the η_{inj} values for $CuBi_2O_4$ and Mg-$CuBi_2O_4$ photocathodes are 24.8% and 36.5%, respectively; at 0.8 V *vs.* RHE, the η_{inj} value for the Mg-$CuBi_2O_4$ photocathode is almost double that of the pristine $CuBi_2O_4$ photocathode (46.7% *vs.* 23.4%). Photo-assisted electrochemical impedance spectroscopy (PEIS) measurements were also performed to analyze the interfacial charge transfer behaviors of $CuBi_2O_4$ and Mg-$CuBi_2O_4$ photocathodes. The collected Nyquist curves shown in Fig. 4h reveal that the charge transfer resistance (R_{ct}) of the pristine $CuBi_2O_4$ photocathode is *ca.* 2 times as large as that of the Mg-$CuBi_2O_4$ photocathode. The above η_{sep}, ΔOCP, η_{inj} and PEIS results together suggest that surface trap states stemming from surface dangling bonds of $CuBi_2O_4$ not only cause Fermi level pinning thereby suppressing charge carrier separation in the $CuBi_2O_4$ film bulk, but also retard water reduction kinetics at the $CuBi_2O_4$ surface, as schemed in Fig. S8a†. Using *in situ* developed MgO segregations, surface traps of the $CuBi_2O_4$ electrode are effectively passivated, giving rise to enhanced charge separation in the bulk and accelerated charge transfer kinetics at the surface of the $CuBi_2O_4$ electrode simultaneously, as illustrated in Fig. S8b.†

IPCE spectra of $CuBi_2O_4$ and Mg-$CuBi_2O_4$ electrodes were measured at 0.6 V *vs.* RHE in KB_i solution. As shown in Fig. 4i, both IPCE curves of $CuBi_2O_4$ and Mg-$CuBi_2O_4$ electrodes exhibit a monotonic decrease trend from 350 to 650 nm, and the onset wavelength of *ca.* 650 nm matches closely with their light absorption curves. Compared to that on the pristine $CuBi_2O_4$ photocathode, the overall profile of the photocurrent action spectrum on the $CuBi_2O_4$ photocathode improves obviously, consistent with the *J–V* measurements in Fig. 1b. The *i–t* curves displayed in Fig. S9† reveal that the water reduction performance of the Mg-$CuBi_2O_4$ photocathode is always higher than that of pristine $CuBi_2O_4$ across the entire test, demonstrating the positive roles of segregated MgO nanoparticles in the Mg-$CuBi_2O_4$ photocathode; the rapid decrease of photocurrents at the initial stage may result from poor water reduction kinetics at the $CuBi_2O_4$ surface. In addition, the results of XRD and SEM demonstrated that the structure and morphology remain stable during the reaction (Fig. S10 and S11†).

Based on the above analyses, the roles played by spontaneously segregated MgO nanoparticles in the Mg-$CuBi_2O_4$ photocathode can be understood as follows. In an ideal case, the photogenerated electrons in the conduction band of p-type $CuBi_2O_4$ would migrate to the electrode surface to drive the

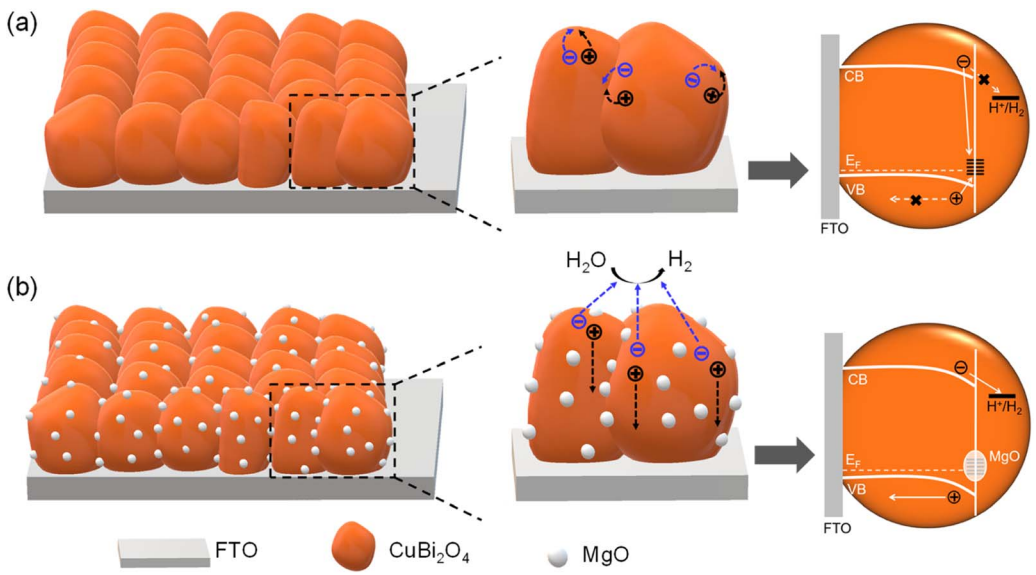

Fig. 5 Schematic diagram of the role of MgO in the PEC water reduction on $CuBi_2O_4$ photocathodes: carrier transport and energy bands of (a) $CuBi_2O_4$ and (b) Mg-$CuBi_2O_4$ photocathodes.

water reduction reaction under the action of the built-in electric field; the photogenerated holes in the valence band would transport to the counter electrode to oxidize water. In practice, to address the issue of mismatched light penetration depths and charge carrier diffusion lengths, nanostructured $CuBi_2O_4$ photocathodes are usually employed and excess dangling bonds are then created on the $CuBi_2O_4$ photocathode surface and form trap states. Under this condition, the built-in electric field (band bending) is deteriorated and photogenerated electrons are easily captured by surface trap states, which lead to increased carrier recombination, delayed photocurrent onset and suppressed saturation photocurrents on nanostructured $CuBi_2O_4$ photocathodes (Fig. 5a). By introducing Mg^{2+} ions in the precursor solution, MgO nanoparticles segregate and enrich at the grain boundaries/surface of the $CuBi_2O_4$ photocathode during the single-pass fabrication procedure. These spontaneously segregated MgO nanoparticles would eliminate (part of) the dangling bonds thereby reducing the trap-state density on the $CuBi_2O_4$ photocathode surface. Under this condition, an enhanced built-in electric field (band bending) and accelerated charge transfer kinetics are achieved on the Mg-$CuBi_2O_4$ photocathode, leading to increased saturation photocurrents and a positively shifted onset potential (Fig. 5b). When used as the passivator, MgO has the following advantages. First, its large bandgap (about 7.8 eV) ensures that MgO will not interfere with the light absorption of $CuBi_2O_4$. Second, MgO exhibits good chemical and electrochemical stability, which would sustain its functions during long-term operation. Third, as an oxyphilic element, Mg would be strongly bonded to oxygen, thus efficiently reducing the density of surface dangling bonds on the $CuBi_2O_4$ photocathode.

Due to its favorable hydrogen-evolution onset potential, the Mg-$CuBi_2O_4$ photocathode was series-connected with a classical Mo-doped $BiVO_4$ photoanode to assemble a bias-free tandem water-splitting device (Fig. 6a). Overlap between the *J*–*V* characteristics of Mg-$CuBi_2O_4$ and Mo:$BiVO_4$ electrodes yields a maximum reachable photocurrent of 0.33 mA cm^{-2} (Fig. 6b), which is increased by 37.5% compared to that of the $CuBi_2O_4$-||Mo:$BiVO_4$ device (Fig. S12†). Under AM 1.5 G simulated sunlight and bias-free conditions, a photocurrent of *ca.* 0.28 mA cm^{-2} is generated on the Mg-$CuBi_2O_4$||Mo:$BiVO_4$ device, demonstrating its ability to drive unbiased overall water splitting (Fig. 6c).

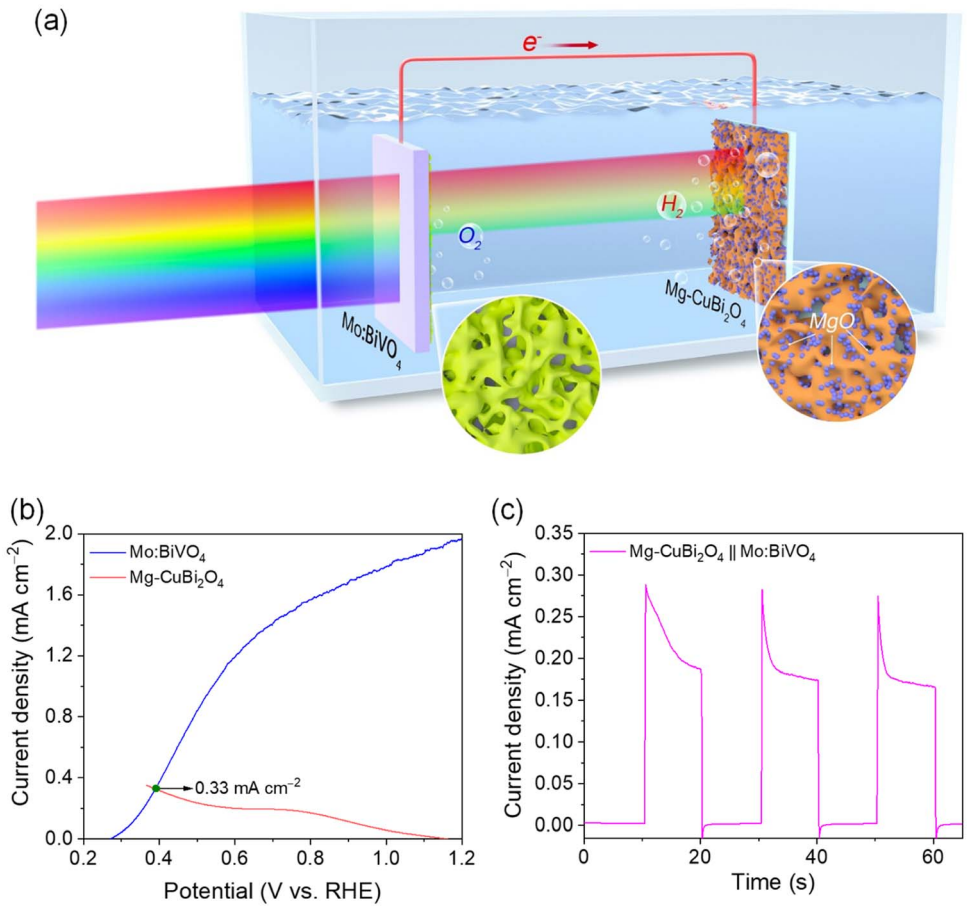

Fig. 6 Performances of the p–n tandem cell: (a) schematic diagram of the Mg-$CuBi_2O_4$||Mo:$BiVO_4$ tandem cell in operation; (b) *J*–*V* curves of a single Mo:$BiVO_4$ photoanode and a single Mg-$CuBi_2O_4$ photocathode; (c) *i*–*t* curve of the p–n tandem cell consisting of Mo:$BiVO_4$ and Mg-$CuBi_2O_4$ under continuous illumination at zero bias voltage.

Conclusions

In summary, an *in situ* surface-trap passivation approach for the $CuBi_2O_4$ photocathode is proposed. It is demonstrated that spontaneously segregated MgO nanoparticles on the $CuBi_2O_4$ photocathode surface partially eliminate surface-trap states, resulting in increased bulk charge separation and improved interfacial charge transfer characteristics. The as-derived MgO(7%)-passivated $CuBi_2O_4$ photocathode yields a photocurrent onset of 1.15 V *vs.* RHE, which is *ca.* 90 mV anodic shift of the pristine $CuBi_2O_4$ photocathode. When the MgO-passivated $CuBi_2O_4$ photocathode is combined with a Mo-doped $BiVO_4$ photoanode to construct a bias-free tandem water-splitting device, a solar-to-hydrogen conversion efficiency of 0.41% is achieved, 37.5% greater than that assembled with a pristine $CuBi_2O_4$ photocathode. This study identifies MgO as a novel yet effective large-bandgap material for passivating surface traps thereby boosting the performances of water-splitting photoelectrodes. Moreover, the concept of *in situ* surface-trap passivation would flourish the passivating strategies for semiconductor-based devices and inspire cost-effective device manufacturing processes.

Experimental

Materials

Bismuth(III) nitrate pentahydrate ($Bi(NO_3)_3\cdot5H_2O$, ≥99.99%, Aladdin Chemistry Co., Ltd); copper(II) nitrate trihydrate ($Cu(NO_3)_2\cdot3H_2O$, ≥99%, Sinopharm Chemical Reagent Co., Ltd); magnesium(II) nitrate hexahydrate ($Mg(NO_3)_2\cdot6H_2O$, ≥99%, Xilong Chemical Co., Ltd); concentrated nitric acid (HNO_3, 65–68%, Sinopharm Chemical Reagent Co., Ltd); glacial acetic acid (CH_3COOH, ≥99.5%, Sinopharm Chemical Reagent Co., Ltd); absolute ethanol (C_2H_6O, ≥99.7%, Sinopharm Chemical Reagent Co., Ltd); boric acid (H_3BO_3, ≥99.5%, Nanjing Chemical Reagent Co., Ltd); potassium hydroxide (KOH, ≥99.7%, Sinopharm Chemical Reagent Co., Ltd) and deionized water were used without further purification.

Preparation of $CuBi_2O_4$ and Mg-modified $CuBi_2O_4$ photocathodes

$CuBi_2O_4$ and Mg-modified $CuBi_2O_4$ photocathodes were synthesized *via* the metal–organic decomposition method (Fig. 1a). $Bi(NO_3)_3\cdot5H_2O$ in glacial acetic acid (0.1 mol L^{-1}), $Cu(NO_3)_2\cdot3H_2O$ in absolute ethanol (0.05 mol L^{-1}) and $Mg(NO_3)_2\cdot6H_2O$ in absolute ethanol (0.05 mol L^{-1}) were used as precursor solutions. For the preparation of the $CuBi_2O_4$ film, a certain amount of Cu and Bi solutions were mixed according to a stoichiometric ratio of Cu : Bi = 1 : 2. Then the mixed solution was dropped on FTO substrates (1 cm × 2 cm), dried at 45 °C and then calcined at 600 °C in a muffle furnace for 60 min to form $CuBi_2O_4$. Mg-modified $CuBi_2O_4$ electrodes were synthesized by adding 1%, 3%, 5%, 7% and 10% of magnesium (with respect to Bi) to the precursor solutions.

Preparation of Mo-doped $BiVO_4$ photoanodes

Mo-doped $BiVO_4$ photoanodes were prepared by a sol–gel method. 1.25 mmol Bi_2O_3 and 1.5 mL HNO_3 were dissolved in 23.5 mL ethylene glycol to obtain 0.1 mol L^{-1} Bi. 2.5 mmol NH_4VO_3 and 1.5 mL HNO_3 were dissolved in 23.5 mL ethylene glycol to form 0.1 mol L^{-1} V. 0.357 mmol $(NH_4)_6Mo_7O_{24}\cdot4H_2O$ was added in 23.5 mL ethylene glycol to produce 0.1 M Mo. The precursor solution of Mo-doped $BiVO_4$ was prepared by mixing 0.2 mmol anhydrous citric acid, 1 mL precursor solution of Bi, and 1 mL precursor solution of V. The mixed solution was dropped on FTO substrates (exposed 1 cm × 1 cm), dried at 90 °C for 20 min, then heated at 120 °C for 20 min, and then calcined at 520 °C for 1 h to synthesize Mo:$BiVO_4$ photoanodes. The $NiFeO_x$ cocatalyst was loaded on Mo:$BiVO_4$ photoanodes by a photo-assisted electrodeposition method. Electrolyte for deposition was potassium borate buffer solution (KOH: 0.2 M; H_3BO_3: 0.4 M) containing 1.5 mmol L^{-1} $FeSO_4\cdot7H_2O$ and 1.5 mmol L^{-1} $Ni(CH_3COO)_2\cdot4H_2O$. The applied potential was at −0.14 V *vs.* Ag/AgCl by the *i–t* testing method. The total time of deposition was 6 min, during which the light was turned off for 20 s after every 30 seconds of illumination.

Characterization of photoelectrodes

The crystal structures of all the photoelectrodes were detected by X-ray diffraction (XRD, Rigaku Ultima III) with Cu Kα radiation ($\lambda = 1.54056$ Å). The light absorption spectra of films were recorded on a UV-visible (UV-vis) spectrophotometer (Shimadzu, UV-vis 2550; PerkinElmer, Lambda 950). The structure of the material and Raman vibrational spectra were measured using a LabRAM ARAMIS Raman spectrometer (HORIBA Scientific). The chemical states of elements were analyzed by X-ray photoelectron spectroscopy (XPS, Thermo ESCALAB 250). The morphologies and elemental distribution of photocathodes were surveyed using a scanning electron microscope (FEI Nova NanoSEM 230 and ZEISS ULTRA 55). High resolution transmission electron microscopy (HRTEM) and selected area electron diffraction (SAED) analysis were investigated using a transmission electron microscope (JEOL 2100F TEM and an FEI double-aberration corrected Titan G2 60-300S/TEM). Surface photovoltage was surveyed using a surface photovoltage spectrometer (CEL-SPS1000). Photoluminescence (PL) and time-resolved photoluminescence (TRPL) decay spectra were observed using a fluorescence spectrometer (Andor-SR-500i).

Electrochemical characterization studies

PEC performances were measured in a three-electrode cell using an electrochemical workstation (CHI-760E, Shanghai Chenhua). The PEC cell consists of a working electrode (photocathode), a reference electrode (Ag/AgCl electrode) and a counter electrode. The electrolyte was a potassium borate buffer solution (KOH: 0.2 M; H_3BO_3: 0.4 M). The potential *vs.* Ag/AgCl was converted to that *vs.* the reversible hydrogen electrode (RHE). Photocurrents were tested under AM 1.5 G simulated sunlight (100 mW cm^{-2}), from a simulator (Newport Sol3A

Class AAA; CEL-AAAS50, Beijing Zhongjiao Jinyuan Technology Co., Ltd). The light intensity was adjusted using a standard silicon cell (Newport 91150).

Author contributions

Yingfei Hu: investigation, methodology, validation, formal analysis, writing – original draft. Jun Wang: methodology, formal analysis, writing – review & editing. Huiting Huang: data curation, methodology, formal analysis, writing – review & editing. Jianyong Feng: formal analysis, supervision, project administration, writing – original draft. Wangxi Liu: data curation, methodology, formal analysis. Hangmin Guan: resources, formal analysis. Lingyun Hao: resources, formal analysis. Zhaosheng Li: supervision, project administration, funding acquisition, writing – review & editing. Zhigang Zou: supervision, project administration, funding acquisition.

Conflicts of interest

The authors declare no competing financial interest.

Acknowledgements

This work was supported by the National Natural Science Foundation of China (No. 22109059, 51902153, and U1663228), National Key Research and Development Program of China (No. 2021YFA1502100 and 2018YFA0209303), Natural Science Foundation of the Jiangsu Higher Education Institutions of China (No. 20KJB430025), Natural Science Foundation of Anhui Provincial (No. 1708085MB42), and Foundations Support from the Jinling Institute of Technology (No. JIT-B-201833, JIT-FHXM-201920, and JIT-B-201903). We thank Yue Xu (Beijing Zhongjiao Jinyuan Technology Co., Ltd) for the surface photovoltage experiment.

References

1 Y. Fang, Y. Zheng, T. Fang, Y. Chen, Y. Zhu, Q. Liang, H. Sheng, Z. Li, C. Chen and X. Wang, *Sci. China: Chem.*, 2020, **63**, 149–181.
2 X. Li, Y. Chen, Y. Tao, L. Shen, Z. Xu, Z. Bian and H. Li, *Chem Catal.*, 2022, **2**, 1315–1345.
3 X. Liu, Y. Zhao, X. Yang, Q. Liu, X. Yu, Y. Li, H. Tang and T. Zhang, *Appl. Catal., B*, 2020, **275**, 119144.
4 J. Li, Z. Lou and B. Li, *Chin. Chem. Lett.*, 2022, **33**, 1154–1168.
5 G. Zhang, Z. Guan, J. Yang, Q. Li, Y. Zhou and Z. Zou, *Sol. RRL*, 2022, **6**, 2200587.
6 L. Pei, H. Cai, H. Jin, T. Li, H. Zhu, Y. Yuan, J. Zhong, S. Yan and Z. Zou, *ChemCatChem*, 2021, **13**, 180–184.
7 M. Wang, G. Zhang, Z. Guan, J. Yang and Q. Li, *Small*, 2021, **17**, e2006952.
8 J. Feng, H. Huang, S. Yan, W. Luo, T. Yu, Z. Li and Z. Zou, *Nano Today*, 2020, **30**, 100830.
9 W. Zhang, Y. Tian, H. He, L. Xu, W. Li and D. Zhao, *Natl. Sci. Rev.*, 2020, **7**, 1702–1725.
10 H. Huang, J. Feng, Z. Li and Z. Zou, *Sci. Bull.*, 2022, **67**, 226–228.
11 X. Wu, C. Y. Toe, C. Su, Y. H. Ng, R. Amal and J. Scott, *J. Mater. Chem. A*, 2020, **8**, 15302–15318.
12 M. A. Lumley, A. Radmilovic, Y. J. Jang, A. E. Lindberg and K. S. Choi, *J. Am. Chem. Soc.*, 2019, **141**, 18358–18369.
13 J.-B. Pan, S. Shen, L. Chen, C.-T. Au and S.-F. Yin, *Adv. Funct. Mater.*, 2021, **31**, 2104269.
14 X. Li, M. Kan, T. Wang, Z. Qin, T. Zhang, X. Qian, Y. Kuwahara, K. Mori, H. Yamashita and Y. Zhao, *Appl. Catal., B*, 2021, **296**, 120387.
15 R.-T. Gao, L. Wu, S. Liu, K. Hu, X. Liu, J. Zhang and L. Wang, *J. Mater. Chem. A*, 2021, **9**, 6298–6305.
16 W. Li, L. Du, Q. Liu, Y. Liu, D. Li and J. Li, *Chem. Eng. J.*, 2020, **384**, 123323.
17 J. Feng, H. Huang, W. Guo, X. Xu, Y. Yao, Z. Yu, Z. Li and Z. Zou, *Chem. Eng. J.*, 2021, **417**, 128095.
18 W. Zhou, J.-K. Guo, S. Shen, J. Pan, J. Tang, L. Chen, C.-T. Au and S.-F. Yin, *Acta Phys.-Chim. Sin.*, 2020, **36**, 1906048.
19 H. Zhu, Q. Yang, D. Liu, Y. Du, S. Yan, M. Gu and Z. Zou, *J. Am. Chem. Soc.*, 2021, **143**, 9236–9243.
20 H. Zhu, S. Xiao, W. Tu, S. Yan, T. He, X. Zhu, Y. Yao, Y. Zhou and Z. Zou, *J. Phys. Chem. Lett.*, 2021, **12**, 10815–10822.
21 H. Quan, Y. Gao and W. Wang, *Inorg. Chem. Front.*, 2020, **7**, 817–838.
22 J. Feng, X. Zhao, B. Zhang, Z. Chen, Z. Li and Y. Huang, *J. Energy Chem.*, 2022, **71**, 20–28.
23 K. Zhang, Y. Lu, Q. Zou, J. Jin, Y. Cho, Y. Wang, Y. Zhang and J. H. Park, *ACS Energy Lett.*, 2021, **6**, 4071–4078.
24 H. Xu, W. Fan, Y. Zhao, B. Chen, Y. Gao, X. Chen, D. Xu and W. Shi, *Chem. Eng. J.*, 2021, **411**, 128480.
25 Y. Song, X. Zhang, Y. Zhang, P. Zhai, Z. Li, D. Jin, J. Cao, C. Wang, B. Zhang, J. Gao, L. Sun and J. Hou, *Angew. Chem., Int. Ed.*, 2022, **61**, e202200946.
26 Q. Wang, L. Wu, Z. Zhang, J. Cheng, R. Chen, Y. Liu and J. Luo, *ACS Appl. Mater. Interfaces*, 2022, **14**, 26642–26652.
27 X. Hu, Y. Li, X. Wei, L. Wang, H. She, J. Huang and Q. Wang, *Adv. Powder Mater.*, 2022, **1**, 100024.
28 J.-B. Pan, B.-H. Wang, J.-B. Wang, H.-Z. Ding, W. Zhou, X. Liu, J.-R. Zhang, S. Shen, J.-K. Guo, L. Chen, C.-T. Au, L.-L. Jiang and S.-F. Yin, *Angew. Chem., Int. Ed.*, 2021, **60**, 1433–1440.
29 Y. Zhao, C. Deng, D. Tang, L. Ding, Y. Zhang, H. Sheng, H. Ji, W. Song, W. Ma, C. Chen and J. Zhao, *Nat. Catal.*, 2021, **4**, 684–691.
30 D. Cao, J. Zhang, A. Wang, X. Yu and B. Mi, *J. Mater. Sci. Technol.*, 2020, **56**, 189–195.
31 P. Liu, C. Wang, L. Wang, X. Wu, L. Zheng and H. G. Yang, *Research*, 2020, **2020**, 1–8.
32 N. Zhang, X. Wang, J. Feng, H. Huang, Y. Guo, Z. Li and Z. Zou, *Natl. Sci. Rev.*, 2020, **7**, 1059–1067.
33 Y. Li, N. Zhang, C. Liu, Y. Zhang, X. Xu, W. Wang, J. Feng, Z. Li and Z. Zou, *Chin. J. Catal.*, 2021, **42**, 1992–1998.
34 J.-B. Pan, X. Liu, B.-H. Wang, Y.-A. Chen, H.-Y. Tan, J. Ouyang, W. Zhou, S. Shen, L. Chen, C.-T. Au and S.-F. Yin, *Appl. Catal., B*, 2022, **315**, 121526.

35 C. Li, J. He, Y. Xiao, Y. Li and J.-J. Delaunay, *Energy Environ. Sci.*, 2020, **13**, 3269–3306.
36 S. P. Berglund, F. F. Abdi, P. Bogdanoff, A. Chemseddine, D. Friedrich and R. van de Krol, *Chem. Mater.*, 2016, **28**, 4231–4242.
37 D. Kang, J. C. Hill, Y. Park and K.-S. Choi, *Chem. Mater.*, 2016, **28**, 4331–4340.
38 A. Song, P. Plate, A. Chemseddine, F. Wang, F. F. Abdi, M. Wollgarten, R. van de Krol and S. P. Berglund, *J. Mater. Chem. A*, 2019, **7**, 9183–9194.
39 D. Huang, K. Wang, L. Li, K. Feng, N. An, S. Ikeda, Y. Kuang, Y. Ng and F. Jiang, *Energy Environ. Sci.*, 2021, **14**, 1480–1489.
40 C. Ma, D.-K. Ma, W. Yu, W. Chen and S. Huang, *Appl. Surf. Sci.*, 2019, **481**, 661–668.
41 N. Xu, F. Li, L. Gao, H. Hu, Y. Hu, X. Long, J. Ma and J. Jin, *ACS Sustainable Chem. Eng.*, 2018, **6**, 7257–7264.
42 A. K. Shah, T. K. Sahu, A. Banik, D. Gogoi, N. R. Peela and M. Qureshi, *Sustainable Energy Fuels*, 2019, **3**, 1554–1561.
43 S. Pulipaka, N. Boni, G. Ummethala and P. Meduri, *J. Catal.*, 2020, **387**, 17–27.
44 Y. Hu, H. Huang, J. Feng, W. Wang, H. Guan, Z. Li and Z. Zou, *Sol. RRL*, 2021, **5**, 2100100.
45 F. Le Formal, N. Tetreault, M. Cornuz, T. Moehl, M. Gratzel and K. Sivula, *Chem. Sci.*, 2011, **2**, 737–743.
46 F. Le Formal, K. Sivula and M. Grätzel, *J. Phys. Chem. C*, 2012, **116**, 26707–26720.
47 J. Brillet, M. Grätzel and K. Sivula, *Nano Lett.*, 2010, **10**, 4155–4160.
48 K. Sivula, F. Le Formal and M. Gratzel, *ChemSusChem*, 2011, **4**, 432–449.
49 Z. Li, J. Feng, S. Yan and Z. Zou, *Nano Today*, 2015, **10**, 468–486.
50 M. Zhong, T. Hisatomi, Y. Kuang, J. Zhao, M. Liu, A. Iwase, Q. Jia, H. Nishiyama, T. Minegishi, M. Nakabayashi, N. Shibata, R. Niishiro, C. Katayama, H. Shibano, M. Katayama, A. Kudo, T. Yamada and K. Domen, *J. Am. Chem. Soc.*, 2015, **137**, 5053–5060.